

Cryogenic mechanical behaviors of CrMnFeCoNi high-entropy alloy

Wujing Fu^{1,2}, Wei Zheng³, Yongjiang Huang^{1,2*}, Fangmin Guo⁴, Songshan Jiang^{1,2},

Peng Xue^{1,2}, Yang Ren⁵, Hongbo Fan^{1,2}, Zhiliang Ning^{2*}, Jianfei Sun²

¹ State Key Laboratory of Advanced Welding and Joining, Harbin Institute of

Technology, Harbin 150001, China

²School of Materials Science and Engineering, Harbin Institute of Technology, Harbin

150001, China

³ Xi'an Space Engine Company Limited, Xi'an 710021, China

⁴College of New Energy and Materials, China University of Petroleum,

Beijing102249, China

⁵X-ray Science Division, Argonne National Laboratory, Argonne, IL, 60439, USA

E-mail: yjhuang@hit.edu.cn; zhiliangning@sina.com

Abstract

The CrMnFeCoNi high-entropy alloy (HEA) exhibits higher yield strength, ultimate strength and ductility at lower temperature. To further clarify the effect of the testing temperature on microstructure evolution, *in-situ* synchrotron-based high-energy X-ray diffraction tensile tests were carried out from 298 K down to 123 K. The enhanced yield strength of the alloy at cryogenic temperatures can be attributed to the greater lattice distortion prior to plastic deformation. Higher strain hardening rate leads to the simultaneously enhanced strength and ductility of the studied HEA below room temperature. Both dynamic Hall-Petch hardening (twinning) and dislocation hardening provide high work hardening capacity for this alloy during the plastic

deformation at cryogenic temperatures. The increased dislocation density and nano-twins at cryogenic temperatures can be attributed to the decrease in the stacking fault energy as the deformation temperature decreases. These studies could provide an in-depth understanding for the strengthening mechanisms of the HEA in different temperature conditions and guide the exploration of HEAs with superb mechanical properties at cryogenic environments.

Keywords: High-entropy alloy; High energy X-ray diffraction; Stacking faults; Nano-twins; Cryogenic temperature

1. Introduction

As a kind of advanced metallic materials, high entropy alloys (HEAs) often comprise five or even more major elements with equal or near-equal molar ratios, which are distinct from the conventional alloys with one or two principal elements. Since their first discovery in 2004 [1, 2], HEAs have arisen considerable practical and scientific interests from researchers due to their excellent combination of high strength and excellent ductility [3-5], strength retention at elevated temperature [6-8], and superior thermal stability induced by their simple and disordered solid-solution structure [9, 10]. Such unique structural features stem from the great lattice distortion and the sluggish diffusion of HEAs in mixing multiple components [11-16].

Recent studies have demonstrated that the mechanical performance of numerous single-phase or dual-phase HEAs can be significantly enhanced with decreasing the testing temperature [17-23], enabling them promising for wide cryogenic applications in the fields such as liquefied gas storage, space exploration and superconductivity. For instance, Otto et al. [17] reported a simultaneous enhancement in both the strength and the ductility of equiatomic CrMnFeCoNi HEA while lowering the test temperature, and attributed such phenomenon to the formation of nano-scale twins during tensile deformation. Xia et al. [18] observed an ultrahigh impact toughness and an abnormal temperature dependence in $\text{Al}_{0.1}\text{CoCrFeNi}$ HEA at the temperature ranging from room temperature to 77 K. For $\text{Fe}_{40}\text{Mn}_{40}\text{Co}_{10}\text{Cr}_{10}$ HEA, Chen et al. [19] ascribed its exceptional low temperature strength to the activated transformation of the martensitic phase and occurrence of twinning at 77 K. Ding et al. [20] also

suggested that CrFeCoNiPd HEA displayed enhanced mechanical properties as the temperature decreased. Transmission electron microscopy (TEM) observations have proven that high strength and ductility of HEAs at cryogenic temperature can be principally attributed to the deformation-induced twinning or/and martensite transformation [17, 24]. In general, the stacking fault energy (SFE) is one of the most significant parameters affecting the propensity to form deformation twins [25-27]. The simulation results have confirmed that the SFE of the CrMnFeCoNi HEA will decrease with decreasing temperature [22], **facilitating** the formation of the cryogenic deformation twins. In order to further validate the simulation results, it is of essence to determine the SFE of the HEA experimentally. X-ray diffraction (XRD) is an effective experimental method for the measurement of SFE [28], especially at cryogenic temperatures. Besides, *in-situ* synchrotron XRD [29] or neutron diffraction [30-34] studies on the alloys can quantify the grain-level behaviors during deformation via calculating the lattice strain [30], SFE [31, 33], and dislocation density [31]. Thus, carrying out the *in-situ* studies on the cryogenic deformation of HEA can validate the numerical simulation results and unravel the complex interaction of dislocations, twins and stacking fault (SF) at cryogenic temperatures.

In this work, *in-situ* high energy X-ray diffraction (HE-XRD) has been used to elucidate the temperature-dependent deformation mechanism in a CrMnFeCoNi HEA subjected to uniaxial tensile stress. The lattice strain and lattice parameters will be calculated to clarify lattice structural evolution, and thus explain the elastic deformation behaviors of this HEA at cryogenic temperatures. Meanwhile, the

formation of twins during the plastic stage will be discussed from the viewpoint of the SF. It is expected that the obtained results can provide more insights for better understanding the deformation mechanisms of HEAs at cryogenic temperatures and thus widening their industrial applications in extreme conditions.

2. Materials and methods

HEA ingots with a nominal composition of CrMnFeCoNi were prepared by arc melting a mixture of high-purity (>99.99 wt. %) raw materials in a Ti-gettered argon atmosphere. Cylindrical samples with 10 mm in diameter and ~60 mm in length were then produced by drop-casting the alloy melt into a copper mold. Dog-bone shaped tensile samples with a gauge length of 7 mm, and a width of 1 mm, and a thickness of 1 mm were electric discharge machined from the cast rod sample, and carefully ground and polished to a mirror surface by SiC paper. Uniaxial tensile loads were applied stepwise to the HEA samples using a displacement-controlled mode until failure after the sample was cooled by liquid nitrogen to desired different temperature and stabilized for 5 minutes.

The HE-XRD measurements were conducted at 11-ID-C beam-line in Advanced Photon Source, Argonne National Laboratory, USA. The schematic illustration of the *in-situ* HE-XRD tensile experimental setup is shown in Fig. 1(a). The wavelength of the monochromatic diffracted X-ray is 0.1173 Å, and the beam energy is 105.7 keV. The sample-to-detector distance is set to 1.6 m using the reference materials CeO₂. A Perkin Elmer amorphous silicon two-dimensional (2-D) detector was used to acquire

diffraction patterns. Each acquisition took 0.1 s. Fig. 1(b) shown the original 2-D diffraction pattern at room temperature. The X-Y plots were obtained by integrating the 2-D diffraction patterns along azimuth angle (η) from 80° to 100° using Dawn software [35, 36]. Single peak fitting in GSAS software package [37] was used to analyze the diffraction data, and thus obtain the information of d -spacing, and full width at half maximum (FWHM) of the studied HEA during tensile deformation.

Here, the shifts of the lattice spacing reflecting the lattice strain of the studied HEA can be calculated using the following equation [38-40]:

$$\varepsilon_{hkl} = \frac{d_{hkl} - d_{hkl,0}}{d_{hkl,0}} \quad (1),$$

where d_{hkl} and $d_{hkl,0}$ is determined from the hkl reflection for a given load and a zero load, respectively.

In order to calculate the dislocation density of the studied HEA, the modified Williamson-Hall plot [41] was used, which is described as follows:

$$\Delta K \equiv \frac{\gamma}{D} + \left(\frac{\pi M^2 b^2}{2} \right) \rho^{1/2} K^2 \bar{C} + O(K^4 \bar{C}^2) \quad (2),$$

where D represents the average grain size or particle size in the specimen, which is obtained from the intercept at $K=0$ of a smooth curve according to Eq. (2) [42]. γ equals to 0.9, b and ρ is the length of the Burgers vector of dislocations, and dislocation density, respectively. M is called dislocation arrangement parameter [41], and $M = Re \times \rho^{1/2}$. Here, Re represents the effective outer cut-off of dislocations, which will be determined from the Fourier coefficients [43, 44]. $\Delta K = \cos \theta [\Delta(2\theta)]/\lambda$, where $\Delta(2\theta)$ is the FWHM of the diffraction curves. K stands for the modulus of the

diffraction vector, equaling $2\sin\theta/\lambda$. O is the higher order terms in $K^4 \bar{C}^2$. \bar{C} is the contrast factors of dislocations, for the cubic polycrystalline material, which can be obtained from the fourth order polynomials of Miller indices [45] as follows:

$$\bar{C} = \bar{C}_{h00}(1 - qH^2) \quad (3),$$

where $H^2 = h^2k^2 + h^2l^2 + k^2l^2/(h^2 + k^2 + l^2)^2$, the values of \bar{C}_{h00} and q can be determined using single crystal elastic constants (SCEC) [45]. For the present CrMnFeCoNi HEA, $c_{11}=200$ GPa, $c_{12}=99$ GPa and $c_{44}=149$ GPa are adopted from the first-principles calculations in Ref. [46].

The phase structure of the as-cast HEA was characterized by Empyrean XRD with CuK α radiation. The scanning electron microscope (HELIOS NanoLab 600i SEM) equipped with an energy-dispersive spectrometer (EDS) was also performed to examine the microstructure of the as-cast samples. Electron backscattered diffraction (EBSD) mapping was carried out to investigate the texture of the as-cast HEA at 30 kV. Quanta 200FEG SEM was used to observe the necked region of the failed specimens after *in situ* tensile deformation. The microstructure of HEA samples after tensile tests was examined using a Talos f-200x TEM operating at 200 kV. TEM foils were cut from the uniformly deformed regions of HEA samples after tensile deformation, carefully ground down to ~ 50 μm thick, and then thinned by twin-jet electro-polishing to ensure the electron transparent.

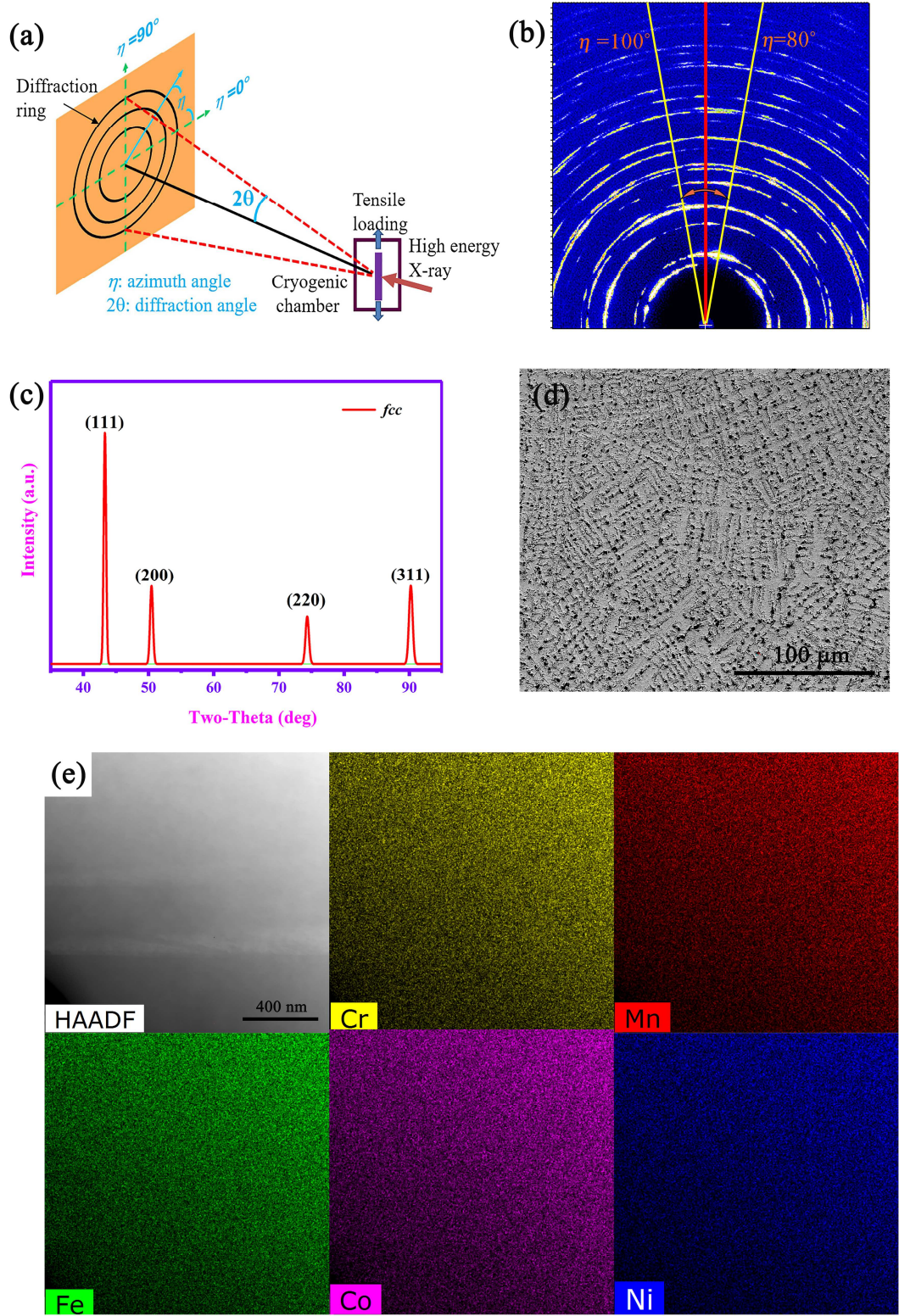


Fig. 1. (a) The schematic of the *in-situ* synchrotron-based HE-XRD experimental set-up at cryogenic temperatures, (b) 2-D diffraction patterns of the HEA at room temperature, (c) a typical XRD pattern, (d) a backscattered electron image of the as-cast CrMnFeCoNi HEA, and (e)

the high-angle annular dark field (HAADF) image and corresponding EDS maps for the individual elements of Cr, Mn, Fe, Co and Ni before deformation.

3. Results

3.1 Mechanical properties in cryogenic environments

Fig. 1(c) plots a typical XRD pattern of the as-cast CrMnFeCoNi HEA, which indicates that the studied alloy using arc melting has a single face-centered cubic (*fcc*) structure. Fig. 1(d) exhibits a typical as-cast dendritic structure of the current HEA. Fig. 1(e) presents the HAADF image from TEM and corresponding EDS maps of the studied CrMnFeCoNi alloy, indicating the equiautomic elemental distribution character.

The EBSD inverse pole figure of the starting CrMnFeCoNi HEA used for tensile deformation is shown in Fig. 2(a). As seen, this cast alloy has grains of ~100 μm average size and weak textures (<2.123 times random) before tensile deformation. These results ensure the validity of the tensile samples during synchrotron radiation experiments.

Fig. 2(b) shows the true stress-strain curves obtained from the uniaxial tensile tests of the studied HEA at 123 K, 173 K, 223 K, and 298 K. As seen in Table I, the cryogenic temperature lead to a remarkable increase in both plasticity and strength of the studied HEA. As tensile deformation proceeds, the stress increases gradually after yielding, suggesting the occurrence of strain strengthening upon tensile loading. Here,

the strain hardening rate (SHR), defined as the derivative of the true stress with respect to the true strain, is introduced to describe the working hardening of the studied HEA. Fig. 2(c) shows SHR value under tensile loading as a function of true stress. As seen, the SHR values for each testing temperature show a similar tendency, with a greater decrease at lower stress but a slower decrease at higher stress. Meanwhile, the SHR of the HEA exhibits the highest value at 123 K but the lowest value at 298 K, suggesting that lower testing temperature can cause higher strain hardening capability for this HEA [47, 48]. The grey area in Fig. 2(c) represents the region ($d\sigma_t/d\varepsilon < \sigma_t$) in which necking occurs according to Considere's criterion [31]. Here, σ_t represents the true stress of the HEA during the tensile testing. With decreasing the testing temperature, the onset of necking in the tensile samples occurs at a progressively higher strain value, which means that the necking of the studied alloy can be remarkably hindered at cryogenic temperatures [17].

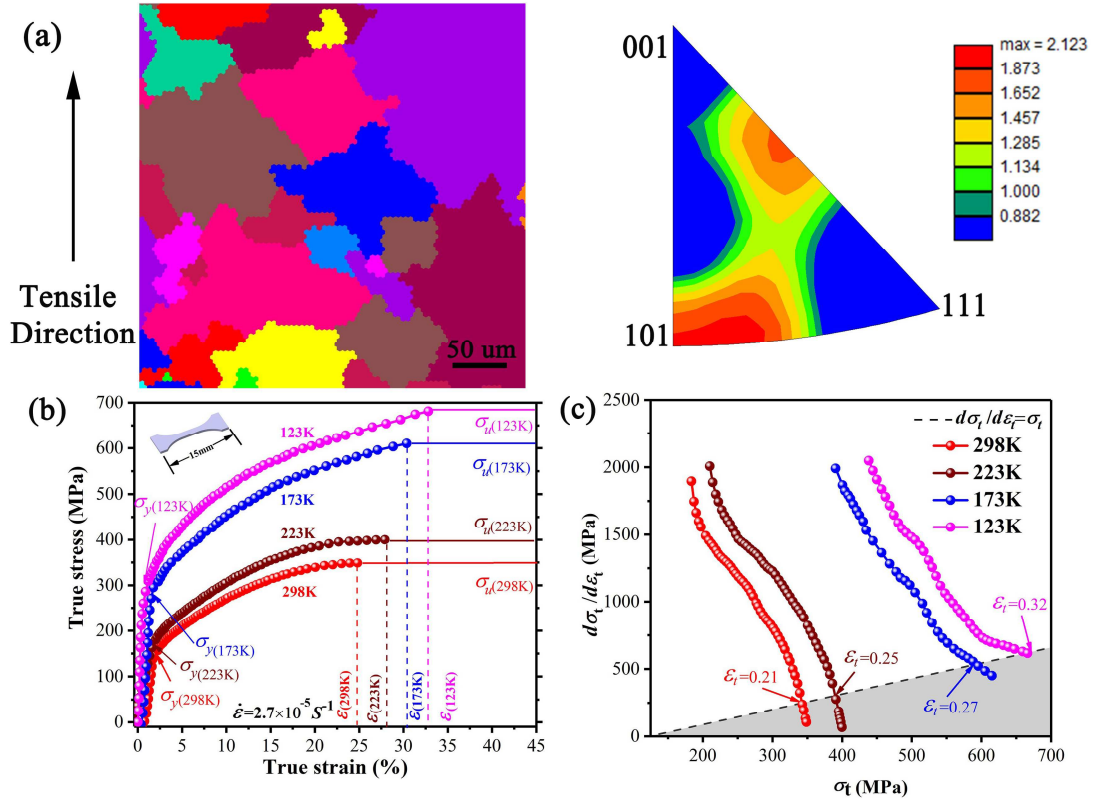


Fig. 2. (a) EBSD inverse pole figure map image of the as-cast CrMnFeCoNi HEA before deformation, (b) true stress-strain curves, and (c) the corresponding strain hardening rate as a function of the true stress at different testing temperatures.

TABLE I The yield strength (σ_y), ultimate strength (σ_u), and tensile plastic strain (ε) of the CrMnFeCoNi HEA obtained at different temperatures.

Temperature (K)	σ_y (MPa)	σ_u (MPa)	ε (%)
298	138	338	25
223	155	400	27
173	300	610	31
123	310	650	33

The fractured surfaces of the HEA after testing at different temperatures are shown in Fig. 3. As seen, the fracture width of the HEA has a significant increase with

decreasing temperature, indicating that the necking gradually becomes less apparent with decreasing temperature [21], agreeing well with the results of Fig. 2(c).

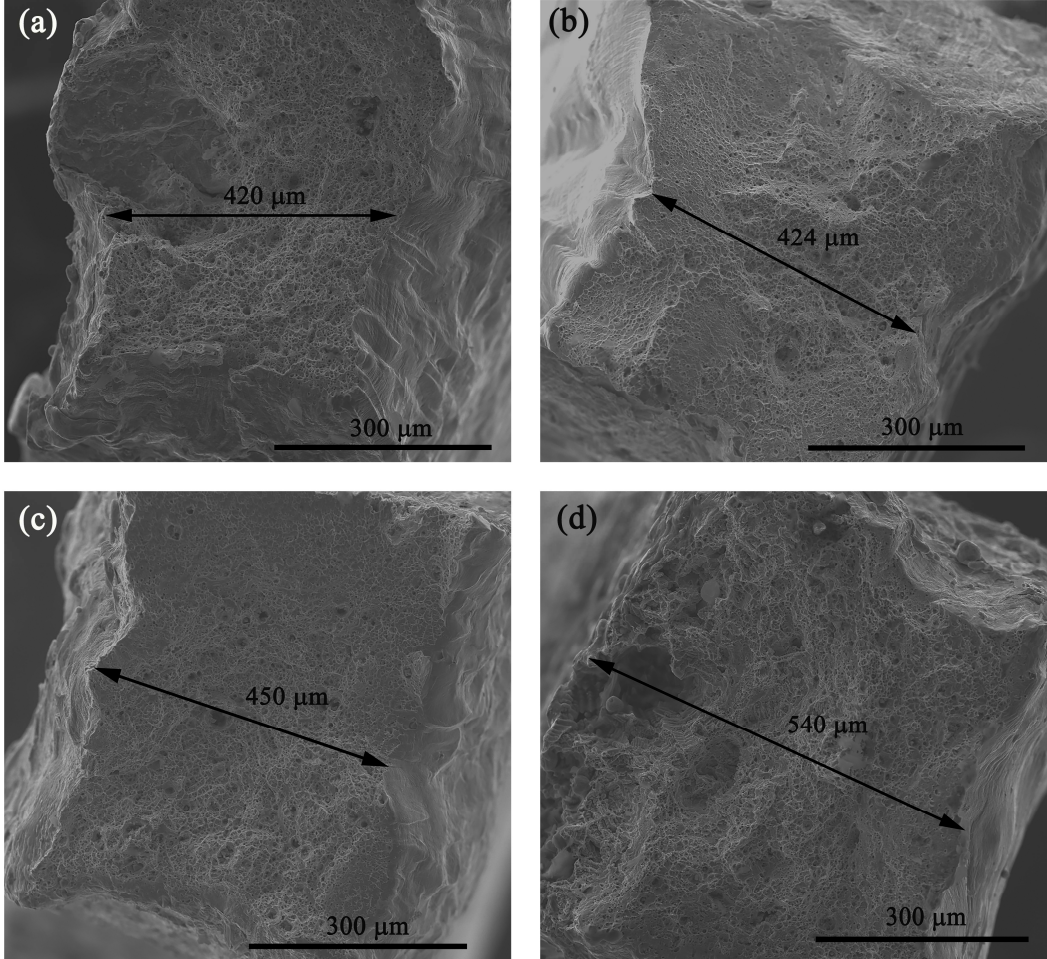


Fig. 3. SEM images of the fractured surfaces of the studied HEA after tensile testing at different temperatures: (a) 298 K, (b) 223 K, (c) 173 K, and (d) 123 K.

3.2 Lattice strain

Fig. 4(a), (b) (c) and (d) plots diffraction patterns of the studied HEA samples along axial direction tested at 123 K, 173 K, 223 K, and 298 K, respectively. Each peak is indexed with the (hkl) diffraction plane at the corresponding d -spacing. As seen, this HEA remains *fcc* structure at different temperatures during loading,

suggesting that no martensitic transformation occurs in this alloy from 298 K down to 123 K. This phenomenon agrees well with the cryogenic tensile deformation results of HEAs in the previous literatures [17, 21].

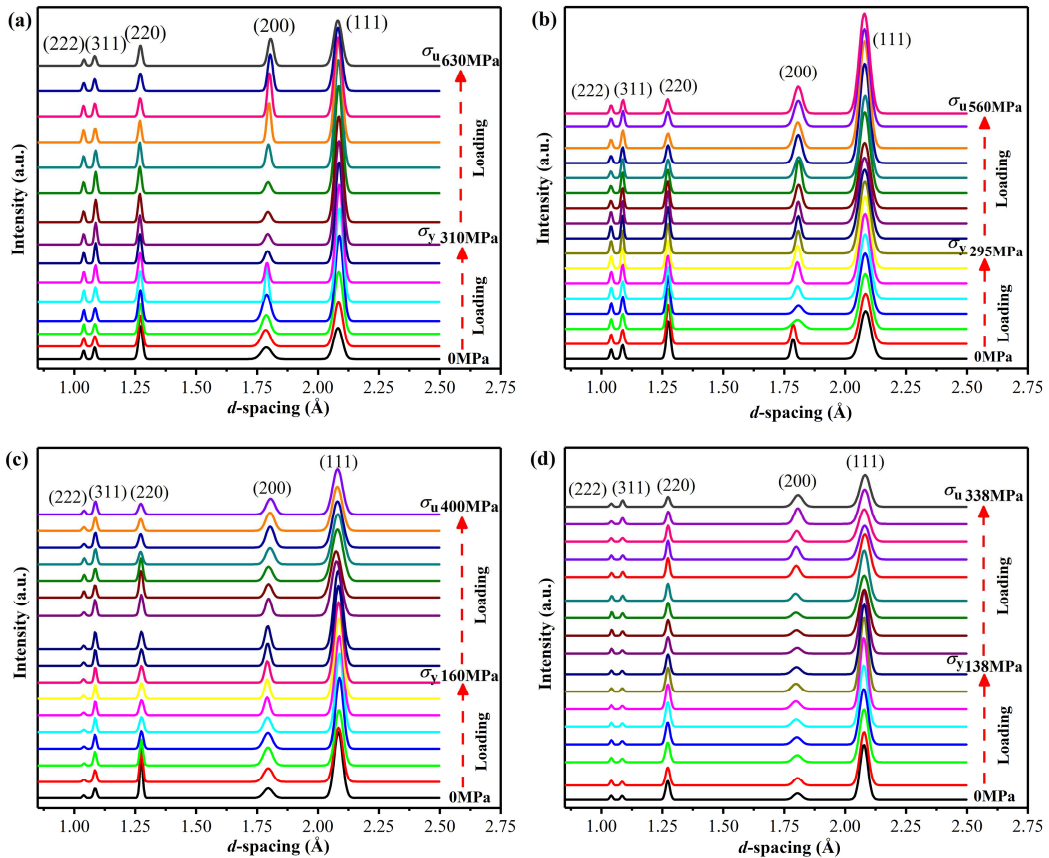


Fig. 4. Diffraction patterns of the CrMnFeCoNi HEA as a function of the applied stress at different temperatures: (a) 123 K, (b) 173 K, (c) 223 K, and (d) 298 K.

According to Eq. (1), the lattice strain values for each applied stress at different temperatures were calculated. The evolution of the lattice strain of the studied HEA at 123 K, 173 K, 223 K and 298 K upon loading is shown in Fig. 5a, 5b, 5c, and 5d, respectively. Noticeably, the true stress-lattice strain curves in (111), (200), (220), (311) and (222) planes can be classified into linear and nonlinear regimes. Once the grain deforms plastically, the lattice strain deviates from the linearity. The yield onset

of the lattice strain at different planes is marked by $\sigma_y^{(hkl)}$. Within the elastic region, the lattice strain depends on the grain orientations, illustrating a strong elastic anisotropy of the studied HEA [30]. It can be seen from Fig. 5(a-d) that, among all the planes, the (200) plane always displays the largest elastic strain whereas the (220) plane has the lowest elastic strain upon loading. Meanwhile, the lattice strain values in all planes at 123K are larger than those at 298K under similar deformation level, suggesting that the current HEA bears higher stress at the lower temperature.

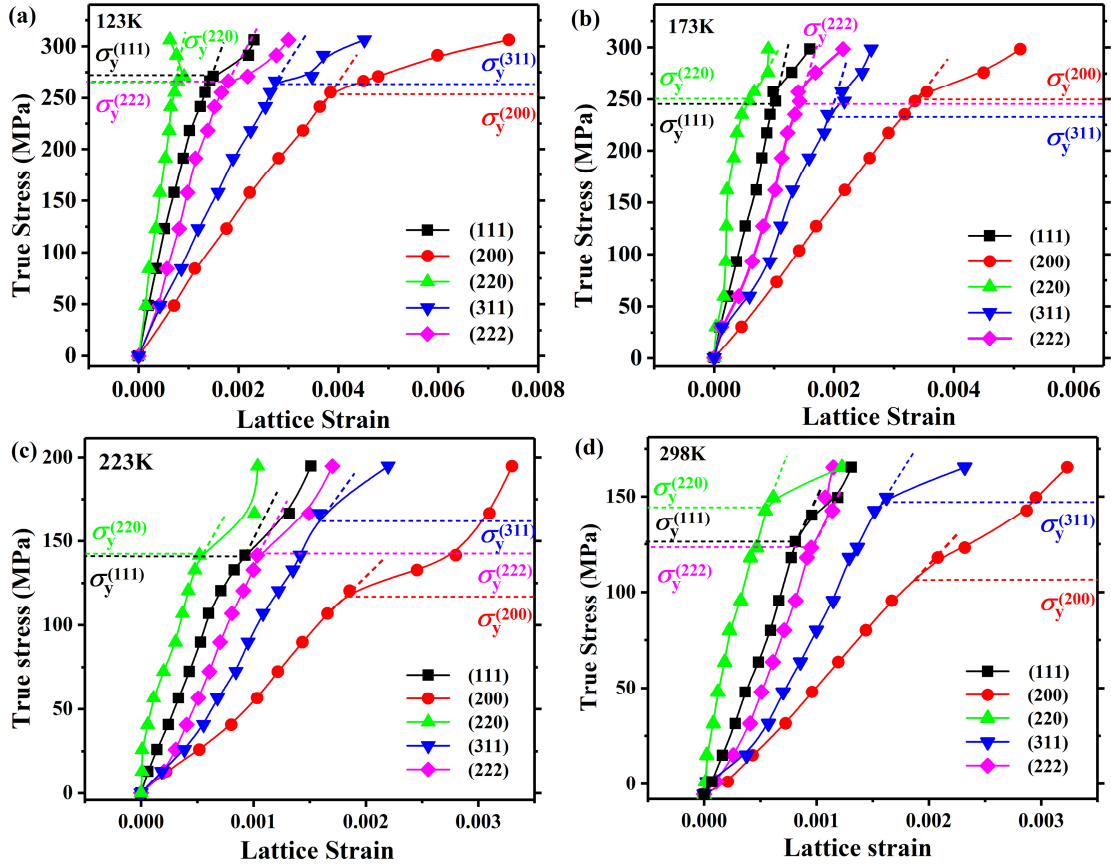


Fig. 5. Evolution of lattice strains of the CrMnFeCoNi HEA as a function of the true stress at (a) 123 K, (b) 173 K, (c) 223 K, and (d) 298 K.

There exists different $\sigma_y^{(hkl)}$ at these stress-lattice strain curves prior to the plastic deformation for all four temperatures, indicating that the strain redistribution arises between the preferentially oriented grains and their neighbors [49]. For the current

HEA, this variation of the lattice strain stems from the fact that the tensile loading can transfer from ‘softer’ grain families, e.g. (220), to ‘harder’ grain families, e.g. (200) [33].

The elastic modulus on various grain orientations can be calculated from the slope of the true stress with respect to the lattice strain. The corresponding calculated values are listed in Table II. It can be noticed from Table II that the {200} directions always have the lowest elastic modulus whereas the {220} directions have the highest value in the studied temperature ranges.

TABLE II. Elastic modulus of differently orientated crystals in the CrMnFeCoNi HEA at different

testing temperatures. (Unit: GPa)

Temperature	$E_{[111]}$	$E_{[200]}$	$E_{[220]}$	$E_{[311]}$
298 K	155	73	279	123
223 K	152	71	272	112
173 K	148	70	270	110
123 K	145	68	268	108

3.3 Lattice parameters

Due to the elastic anisotropy in *fcc* CrMnFeCoNi HEA, various orientations exhibit significantly different lattice strain during elastic deformation, as shown in Fig. 6. The change of lattice parameters during deformation can reflect the lattice distortion of the crystals caused by the elastic anisotropy of the lattice strain [50]. Fig. 6 shows the lattice parameters as a function of true stress at different temperatures

prior to plastic deformation. As seen, the lattice parameter increases from 0.35293 nm at 123 K to 0.35362 nm at 298 K in a stress-free state. This means that the cryogenic condition will result in a smaller lattice parameter. The difference in lattice parameters between the yielding and stress-free state is defined as Δa in Fig. 6. The Δa value dramatically increases with decreasing the testing temperature, suggesting that the studied HEA exhibits larger lattice distortion during tensile deformation at cryogenic temperature than that at room temperature.

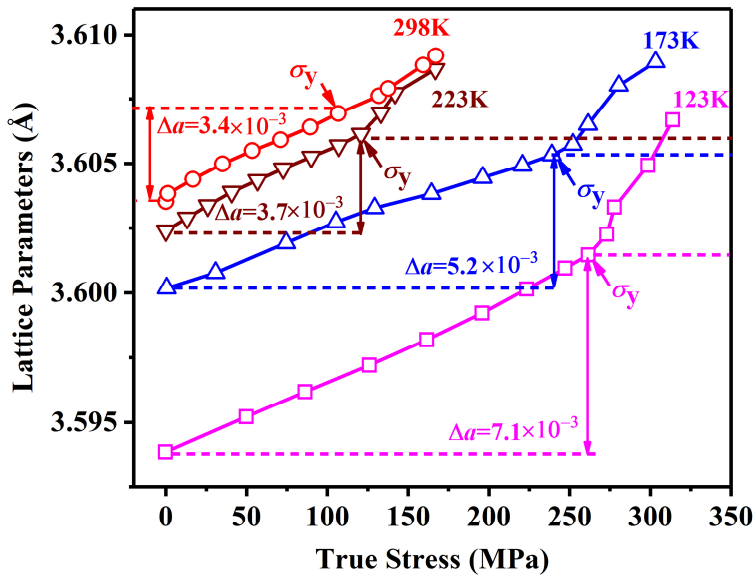


Fig. 6. Evolution of lattice parameters as a function of true stress in the CrMnFeCoNi HEA at different testing temperatures.

4. Discussion

4.1 Lattice distortion

As aforementioned, the elastic strain redistribution between the (200) planes and (220) planes occurs significantly in this alloy during the tensile deformation. However, this redistribution takes place at a higher stress (250 MPa) at 123K than that at 298K

(120 MPa). The excessive stretching may weaken the interatomic bonding in (200) planes prior to the plastic deformation in (220) planes, and then accelerate the nucleation of vacancies [50]. The over-saturated vacancies can facilitate the formation of vacancy clusters or micro-voids during continuous deformation, preventing the slipping of dislocations [51]. Furthermore, accelerated stretching in (200) planes may aggravate the lattice distortion in the crystal structure. As shown in Fig. 6, the Δa value of the studied HEA is larger at cryogenic temperatures than room temperature. Such a large lattice distortion in the current alloy may increase the Peierls-barrier stress and thus hinder the nucleation of dislocations on {111} grains [52]. Overall, the nucleation and slipping of dislocations will become more difficult at cryogenic temperatures than at room temperature. The suppression of dislocation slipping is not conducive to the plastic deformation of the HEA, which unravels the underlying mechanism of the pronounced yield strength at cryogenic temperatures, as shown in Fig. 2 (c).

4.2 Deformation induced nano-twins

Both the ultimate strength and plasticity of the studied HEA also increase dramatically with decreasing the testing temperature (Fig. 2(b)). To further unveil the plastic deformation mechanism of the studied HEA at different temperatures, the microstructure of the deformed specimens after the *in-situ* HE-XRD tensile studies are examined by TEM. Fig. 7 shows the bright-field (BF) TEM images and selected area diffraction patterns (SADP) of the fractured HEA samples at 298 K and 123 K.

Numerous dislocations can be observed in Fig. 7(a), suggesting that the deformation behavior is mainly dominated by dislocation slipping at room temperature. Apart from the profuse dislocations, the nano-sized lamellar structure is also found in Fig. 7(b), which are confirmed as twinning by SADP (Fig. 7(d)). This implies that the twinning is also an important plastic deformation mode of the HEA at 123 K. Nano-twins induced by deformation introduce new interfaces and decrease the mean free path of dislocations (dynamic “Hall-Petch”) for this HEA during the plastic deformation [17, 48]. Meanwhile, no martensite phase can be detected in TEM images, consistent with the HE-XRD results shown in Fig. 4.

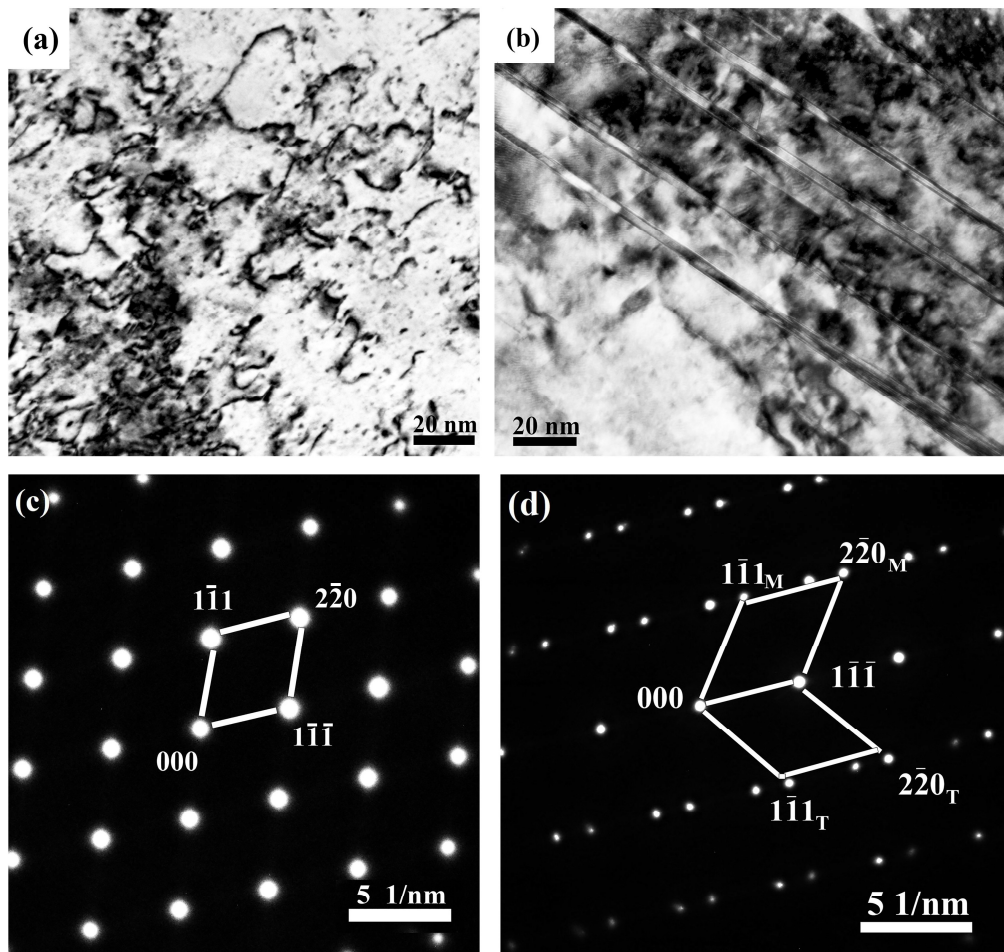


Fig. 7. Bright-field TEM images at (a) 298 K, and (b) 123 K; and corresponding selected area

diffraction patterns along the [110] zone axis of the CrMnFeCoNi HEA after tensile deformation

at (c) 298 K, and (d) 123 K.

As aforementioned, deformation at cryogenic temperature will cause a larger SHRs (Fig. 2c), attributable to the combination of enhanced dislocation hardening and deformation-induced twinning. Such increased work hardening contributes to the dramatic increase in both strength and plasticity of the studied HEA at cryogenic conditions.

4.3 Dislocation density

Dislocations slipping dominates the plastic deformation mechanism in *fcc* matrix [51-53]. For the studied HEA, the higher SHR at cryogenic temperature can be attributed to the interaction between dislocation and nano-twins [17]. Here, the dislocation density at different temperatures is calculated using Eq. (2), and depicted in Fig. 8. As seen, the dislocation density almost linearly increases with increasing the true strain. This tendency can be described using the following equation:

$$\rho = \rho_0 + K\epsilon \quad (4),$$

where K represents the slope of the curves in Fig. 8, ρ_0 is dislocation density at stress-free state, and ϵ is true strain of the current HEA during tensile deformation.

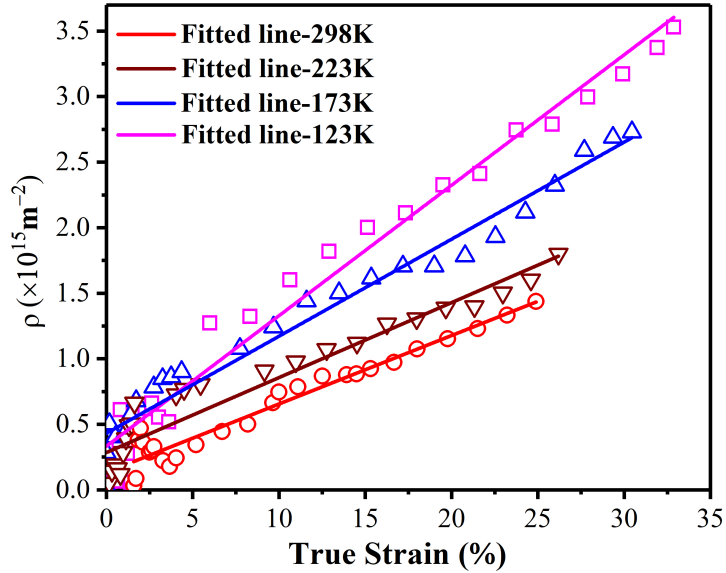


Fig. 8. The evolution dislocation density as a function of true strain at different temperatures.

Based on Eq. (4), the values of ρ_0 and K at different temperatures are listed in Table III. As shown, the value of K increases from 0.052 at 298 K to 0.099 at 123 K, indicating that the higher dislocation density will be accumulated in this HEA after plastic deformation at cryogenic temperatures.

TABLE III. The values of ρ_0 and K of the CrMnFeCoNi HEA at different temperatures

Temperature(K)	ρ_0 ($\times 10^{15}$)	K ($\times 10^{18}$)
298	0.23	0.052
223	0.26	0.057
173	0.28	0.071
123	0.3	0.099

4.4 Stacking fault probability and stacking fault energy

Nanoscale twins can be found in 123K fractured HEA sample. However, no such phenomenon occurs when tested at 298K. This suggests that testing temperature

exerts a crucial role in the plastic deformation behaviors of the current HEA. Twinning is a kind of plastic deformation mode in materials under shear stress, adjusting the direction of slipping, and thus introducing the new slip system [54]. For *fcc* metals, the SF plays a significant role in the competition between slipping and twinning [55-57]. Here, the SF is introduced to reveal the formation mechanism of the nano-twins. During plastic deformation, a perfect dislocation with a Burgers vector $a/2\langle 110 \rangle$ may split into a couple of Shockley partial dislocations with $a/6\langle 112 \rangle$ in *fcc* alloys and generate an SF region with lower mismatch energy. Continuous passages of the partial dislocations on successive (111) planes can create multi-layer SF, facilitating twin nucleation during the plastic deformation [55]. Several studies have stated that SF contributes to the diffraction peak shifts [56, 58]. The discrepancy between the lattice strains of the $\{111\}$ grains and $\{222\}$ grains is attributed to the occurrence of SF [31]. Here, the stacking fault probability (SFP) can be calculated using the simplified equation [54] as follows:

$$SFP = \frac{32\pi}{3\sqrt{3}} (\varepsilon_{222} - \varepsilon_{111}) \quad (5),$$

where $\varepsilon_{(222)}$ and $\varepsilon_{(111)}$ represent the lattice strain in (222) and (111) planes, respectively.

Fig. 9 plots the SFP under tensile loading for the CrMnFeCoNi HEA at different temperatures. As shown in Fig. 9, the SFP varies appreciably as the true strain increases in the investigated temperature range. Here, the evolution of SFP during loading at different temperatures is fitted using the linear function. Two distinct features can be observed from the fitting curves: (i) the slope of the SFP curves

increases with decreasing the temperature, and (ii) at an identical strain level, the cryogenic temperature will result in a much higher SFP value compared with room temperature. Based on the above analysis, we conclude that more SF may form in the HEA tensile samples, and the nano-twins may nucleate and grow quicker under an identical deformation level at cryogenic temperature, compared with room temperature.

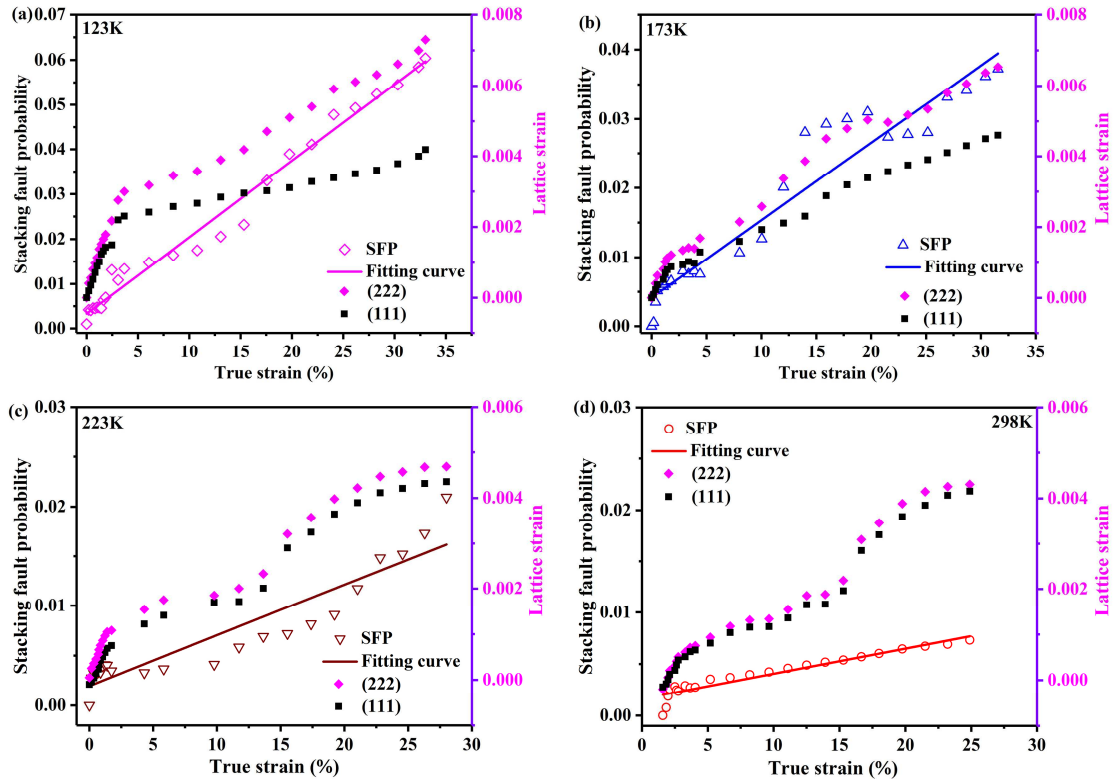


Fig. 9. The SFP in the CrMnFeCoNi HEA as a function of true strain at (a) 123 K, (b) 173 K, (c) 223 K, and (d) 298 K.

The SFE value can reflect whether the SF forms in crystal structure during plastic deformation or not [25, 26]. In the present work, the SFE can be described using Reed and Schramm's equation [58] as follows:

$$SFE = \frac{6.6a_0}{\pi\sqrt{3}} \left(\frac{2c_{44}}{c_{11} - c_{12}} \right)^{-0.37} \frac{\langle \xi_{50}^2 \rangle_{111}}{SFP} \left(\frac{c_{44} + c_{11} - c_{12}}{3} \right) \quad (6)$$

where a_0 is the lattice parameter in a stress-free state. $\langle \xi_{50}^2 \rangle_{111}$ is the root-mean-square micro-strain in the [111] direction averaged over a distance of 50 Å [58], which can be calculated using the order dependent Lorentzian and Gaussian component of integral breadths and Fourier length (L) as follows [59]:

$$\langle \xi^2(L) \rangle = \frac{[1 - \exp(-2L\beta_L - \pi L^2 \beta_G^2)]}{2\pi^2 s^2 L^2} \quad (7),$$

where s represents the reciprocal of the interplanar distance of the HEA. β_L and β_G are constant parameters of the single peak fitting function (Voigt function) in this work. Here, the SCEC ($c_{11}=200$ GPa, $c_{12}=99$ GPa and $c_{44}=149$ GPa) are adopted from first-principles calculations on the CrMnFeCoNi HEA [46]. For this HEA, the simulation results have proven that SCEC varies slightly with decreasing the temperature [22]. Thus, in this work, the SFE of the HEA at different temperatures is calculated using the same SCEC.

The SFE of the studied CrMnFeCoNi HEA at different temperatures is calculated using Eq. (6) at a true strain level of 25%, as depicted in Fig. 10. At room temperature, the calculated SFE in this work is 29.8 mJ/m², close to the measurements by the combination of XRD and simulation (18.3~27.3 mJ/m²) [46] or TEM (26.5 ± 4.5 mJ/m²) [28]. Meanwhile, the SFE of the studied HEA has a remarkable decrease as the deformation temperature decreases (Fig. 10), which is consistent with the *ab initio* results [22].

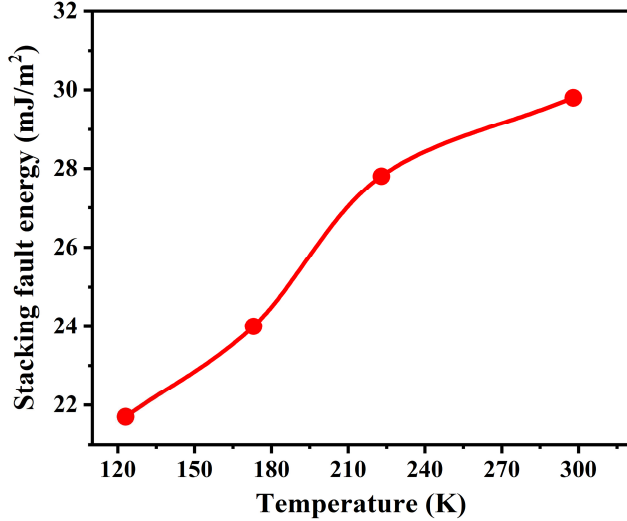


Fig. 10. Stacking fault energy of CrMnFeCoNi HEA from 298 K cooling down to 123 K at a true strain of 25%.

Therefore, lowering the deformation temperature significantly reduces SFE, demonstrating that CrMnFeCoNi HEA is more likely to deform by twinning [46], and agreeing well with the TEM observations in Fig. 7(b). Additionally, in an alloy with lower SFE, a perfect dislocation easily splits into partial dislocations, causing a larger width of the stacking fault (partial dislocation spacing). The dislocation cross-slipping and climbing will be suppressed as the SF width increases [53]. In a word, the decrease of SFE at cryogenic temperatures facilitates the nucleation and growth of twins in the studied HEA. The twinning can lead to the enhancement of both the strength and plasticity of the studied HEA.

5. Conclusions

In-situ synchrotron-based HE-XRD tensile tests, coupled with electron microscopy observations, have been performed to study the microstructural evolution

of the HEA as the testing temperature decreases from 298 K to 123 K. The following conclusions can be drawn:

1. From *in-situ* tensile results, the ultimate strength, yield strength and ductility of the CrMnFeCoNi HEA increase remarkably from 298 K down to 123 K. A higher SHR is also obtained at cryogenic temperature than that at room temperature.

2. The lattice structure of CrMnFeCoNi HEA during elastic deformation is deviated considerably from the initial crystal structure below room temperature, indicating a severe deformation of the lattice structure prior to plastic deformation. Large distortion in the crystal structure can increase the Peierls-barrier stress and hinder the dislocation nucleation, enhancing yield strength of the HEA at cryogenic temperatures.

3. Dislocation density is higher at cryogenic temperature than that at room temperature. Meanwhile, deformation-induced nano-twins are also observed in the fractured samples at 123 K, suggesting that the deformation mechanism of the HEA is mainly dominated by dislocation slipping and twinning at cryogenic conditions.

4. Using HE-XRD diffraction line profile analysis, the SFP and SFE of the CrMnFeCoNi HEA are calculated during the tensile loading at different temperatures. At cryogenic temperatures, the SFP increases quicker and reaches a higher value at an identical true strain than that at room temperature. The SFE of the studied HEA decreases significantly with decreasing temperature, implying that the current alloy upon loading may form more SFs and twins at lower temperatures.

5. Both dynamic Hall-Petch hardening and dislocation hardening can provide

high work hardening capacity for this HEA during the plastic deformation at cryogenic temperatures. Such a pronounced work hardening leads to the dramatic increase of strength and plasticity in the studied HEA below room temperature.

Acknowledgments

This work was financially supported by the National Natural Science Foundation of China (NSFC) under Grant Nos. 51871076, 51671070, and 51827801. This research used resources of the Advanced Photon Source, a U.S. Department of Energy (DOE) Office of Science User Facility operated for the DOE Office of Science by Argonne National Laboratory under Contract No. DE-AC02-06CH11357.

References

- [1] B. Cantor, I.T.H. Chang, P. Knight, A.J.B. Vincent, Microstructural development in equiatomic multicomponent alloys, *Mater. Sci. Eng. A* 375-377 (2004) 213-218.
- [2] J.W. Yeh, S.K. Chen, S.J. Lin, J.Y. Gan, T.S. Chin, T.T. Shun, C.H. Tsau, S.Y. Chang, Nanostructured high-entropy alloys with multiple principal elements: novel alloy design concepts and outcomes, *Adv. Eng. Mater.* 6 (2004) 299-303.
- [3] Y. Zhang, T.T. Zuo, Z. Tang, M.C. Gao, K.A. Dahmen, P.K. Liaw, Z.P. Lu, Microstructures and properties of high-entropy alloys, *Prog. Mater. Sci.* 61 (2014) 1-93.
- [4] D.B. Miracle, O.N. Senkov, A critical review of high entropy alloys and related concepts, *Acta Mater.* 122 (2017) 448-511.
- [5] Z.M. Li, K.G. Pradeep, Y. Deng, D. Raabe, C.C. Tasan, Metastable high-entropy dual-phase

alloys overcome the strength-ductility trade-off, *Nature* 534 (2016) 227-230.

- [6] J.B. Li, B. Gao, S. Tang, B. Liu, Y. Liu, Y.T. Wang, J.W. Wang, High temperature deformation behavior of carbon-containing FeCoCrNiMn high entropy alloy. *J. Alloys Compd.* 747 (2018) 571-579.
- [7] A. Gali, E.P. George, Tensile properties of high- and medium-entropy alloys, *Intermetallics* 39 (2013) 74-78.
- [8] J.H. Kim, K.R Lim, J.W. Won, Y.S. Na, H.-S. Kim, Mechanical properties and deformation twinning behavior of as-cast CoCrFeMnNi high-entropy alloy at low and high temperatures, *Mater. Sci. Eng. A* 712 (2018) 108-113.
- [9] G. Bracq, M. Laurent-Brocq, L. Perrière, R. Pirès, J.M. Joubert, I. Guillot, The *fcc* solid solution stability in the Co-Cr-Fe-Mn-Ni multi-component system, *Acta Mater.* 128 (2017) 327-336.
- [10] F. Otto, A. Dlouhý, K.G. Pradeep, M. Kuběnová, D. Raabe, G. Eggeler, E.P. George, Decomposition of the single-phase high-entropy alloy CrMnFeCoNi after prolonged anneals at intermediate temperatures, *Acta Mater.* 112 (2016) 40-52.
- [11] M.H. Tsai, J.W. Yeh, High-entropy alloys: A critical review, *Mater. Res. Lett.* 2 (2014) 107-123.
- [12] O.N. Senkov, G.B. Wilks, D.B. Miracle, C.P. Chuang, P.K. Liaw, Refractory high-entropy alloys, *Intermetallics*, 18 (2010) 1758-1765.
- [13] K.Y. Tsai, M.H. Tsai, J.W. Yeh, Sluggish diffusion in Co-Cr-Fe-Mn-Ni high-entropy alloys, *Acta Mater.* 61 (2013) 4887-4897.
- [14] A.G. Wang, X.H. An, J. Gu, X.G. Wang, L.L. Li, W.L. Li, M. Song, Q.Q. Duan, Z.F. Zhang,

X.Z.Liao. Effect of grain size on fatigue cracking at twin boundaries in a CoCrFeMnNi high-entropy alloy. *J. Mater. Sci. Technol.* 39 (2020) 1-6

[15] T. Zhang, L.J. Xin, F.F. Wu, R.D. Zhao, J. Xiang, M.H. Chen, S.S. Jiang, Y.J. Huang, S.H. Chen. Microstructure and mechanical properties of Fe_xCoCrNiMn high-entropy alloys. *J. Mater. Sci. Technol.* 35 (2019) 2331-2335

[16] T. Zhang, R.D. Zhao, F.F. Wu, S.B. Lin, S.S. Jiang, Y.J. Huang, S.H. Chen, J.Eckert. Transformation-enhanced strength and ductility in a FeCoCrNiMn dual phase high-entropy alloy. *Mater. Sci. Eng. A* 780 (2020) 139182

[17] F. Otto, A. Dlouhý, Ch. Somsen, H. Bei, G. Eggeler, E.P. George, The influences of temperature and microstructure on the tensile properties of a CoCrFeMnNi high-entropy alloy, *Acta Mater.* 61 (2013) 5743-5755.

[18] S.Q. Xia, M.C. Gao, Y. Zhang, Abnormal temperature dependence of impact toughness in Al_xCoCrFeNi system high entropy alloys, *Mater. Chem. Phys.* 210 (2018) 213-221.

[19] L.B. Chen, R. Wei, K. Tang, J. Zhang, F. Jiang, J. Sun, Ductile-brittle transition of carbon alloyed Fe₄₀Mn₄₀Co₁₀Cr₁₀ high entropy alloys, *Mater. Lett.* 236 (2019) 416-419.

[20] Q.Q. Ding, X.Q. Fu, D.K. Chen, H.B. Bei, B. Gludovatz, J.X. Li, Z. Zhang, E.P. George, Q. Yu, T. Zhu, R.O. Ritchie, Real-time nanoscale observation of deformation mechanisms in CrCoNi-based medium- to high-entropy alloys at cryogenic temperatures, *Mater. Today* 25 (2019) 21-27.

[21] B. Gludovatz, A. Hohenwarter, D. Catoor, E.H. Chang, E.P. George, R.O. Ritchie, A fracture-resistant high-entropy alloy for cryogenic applications, *Science* 345 (2014) 1153-1158.

- [22] S. Huang, W. Li, S. Lu, F.Y. Tian, J. Shen, E. Holmström, L. Vitos, Temperature dependent stacking fault energy of FeCrCoNiMn high entropy alloy, *Scr. Mater.* 108 (2015) 44-47.
- [23] Z.F. He, N. Jia, D. Ma, H.L. Yan, Z.M. Li, D. Raabe, Joint contribution of transformation and twinning to the high strength-ductility combination of a FeMnCoCr high entropy alloy at cryogenic temperatures, *Mater. Sci. Eng. A* 759 (2019) 437-447.
- [24] Q.Y. Lin, J.P Liu, X.H. An, H. Wang, Y. Zhang, X. Z Liao, Cryogenic-deformation-induced phase transformation in an FeCoCrNi high-entropy alloy, *Mater. Res. Lett.* 6 (2018) 236-243.
- [25] Y.L. Gong, C.E. Wen, X.X. Wu, S.Y. Ren, L.P. Cheng, X.K. Zhu, The influence of strain rate, deformation temperature and stacking fault energy on the mechanical properties of Cu alloys, *Mater. Sci. Eng. A* 583 (2013) 199-204.
- [26] K. Youssef, M. Sakaliyska, H. Bahmanpour, R. Scattergood, C. Koch, Effect of stacking fault energy on mechanical behavior of bulk nanocrystalline Cu and Cu alloys, *Acta Mater.* 59 (2011) 5758-5764.
- [27] S.F. Liu, Y. Wu, H.T. Wang, J.Y. He, J.B. Liu, C.X. Chen, X.J. Liu, H. Wang, Z.P. Lu, Stacking fault energy of face-centered-cubic high entropy alloys, *Intermetallics* (93) 2018 269-273.
- [28] D. Rafaja, C. Krötschek, C. Ullrich, S. Martin, Stacking fault energy in austenitic steels determined by using *in situ* X-ray diffraction during bending, *J. Appl. Cryst.* (47) 2014 936-947.
- [29] L.L. Ma, L. Wang, Z.H. Nie, F.C. Wang, Y.F. Xue, J.L. Zhou, T.Q. Cao, Y.D. Wang, Y. Ren, Reversible deformation-induced martensitic transformation in $\text{Al}_{0.6}\text{CoCrFeNi}$ high-entropy alloy investigated by *in-situ* synchrotron-based high-energy X-ray diffraction. *Acta Mater.*

128 (2017) 12-21.

- [30] Y. Wu, W.H. Liu, X.L. Wang, D. Ma, A.D. Stoica, T.G. Nieh, Z.B. He, Z.P. Lu, *In-situ* neutron diffraction study of deformation behavior of a multi-component high-entropy alloy. *Appl. Phys. Lett.* 104 (2014) 51910.
- [31] Y.Q. Wang, B. Liu, K. Yan, M.S. Wang, S. Kabra, Y. L. Chiu, D. Dye, P. D. Lee, Y. Liu, B. Cai, Probing deformation mechanisms of a FeCoCrNi high-entropy alloy at 293 and 77 K using *in-situ* neutron diffraction, *Acta Mater.* 154 (2018) 79-89.
- [32] W. Woo, E.W. Huang, J. W. Yeh, H. Choo, C. Lee, S.Y. Tu. *In-situ*, neutron diffraction studies on high-temperature deformation behavior in a CoCrFeMnNi high entropy alloy. *Intermetallics* 62 (2015) 1-6.
- [33] B. Cai, B. Liu, S. Kabra, Y.Q. Wang, K. Yan, P.D. Lee, Y. Liu. Deformation mechanisms of Mo alloyed FeCoCrNi high entropy alloy: *in-situ* neutron diffraction. *Acta Mater.* 127 (2017) 471-480.
- [34] M. Naeem, H.Y. He, F. Zhang, H.L. Huang, S. Harjo, T. Kawasaki, B. Wang, S. Lan, Z.D. Wu, F. Wang, Y. Wu, Z.P. Lu, Z.W. Zhang, C. T. Liu, X.L. Wang, Cooperative deformation in high-entropy alloys at ultralow temperatures. *Sci. Adv.* 6 (2020) 1-8.
- [35] M. Basham, J. Filik, M.T. Wharmby, P.C.Y. Chang, B. E. Kassaby, M. Gerring, J. Aishima, K. Levik, B.C.A. Pulford, I. Sikharulidze, D. Sneddon, M. Webber, S.S. Dhesi, F. Maccherozzi, O. Svensson, S. Brockhauser, G. Náray, A.W. Ashton. Data analysis workbench (DAWN), *J. Synchrotron Rad.* 22 (2015) 853-858.
- [36] J. Filik, A.W. Ashton, P.C.Y. Chang, P.A. Chater, S.J. Day, M. Drakopoulos, M.W. Gerring, M.L. Hart, O.V. Magdysyuk, S. Michalik, A. Smith, C.C. Tang, N.J. Terrill, M.T. Wharmby, H. Wilhelm, Processing two-dimensional X-ray diffraction and small-angle scattering data

- in DAWN 2, J. Appl. Cryst. 50 (2017) 959-966.
- [37] B.H. Toby, EXPGUI, a graphical user interface for GSAS, J. Appl. Cryst. 34 (2001) 210-213.
- [38] K. An, H.D. Skorpenske, A.D. Stoica, D. Ma, X.L. Wang, E. Cakmak, First *in-situ* lattice strains measurements under load at VULCAN, Metall. Mater. Trans. A 42A (2011) 95-99.
- [39] K.D. Liss, A. Bartels, H. Clemens, S. Bystrzanowski, A. Stark, T. Buslaps, F.P. Schimansky, R. Gerling, C. Scheu, A. Schreyer, Recrystallization and phase transitions in a γ -TiAl-based alloy as observed by *ex situ* and *in-situ* high-energy X-ray diffraction, Acta Mater. 54 (2006) 3721-3735.
- [40] X.L. Wang, Y.D. Wang, A.D. Stoica, D.J. Horton, H. Tian, P.K. Liaw, H. Choo, J.W. Richardson, E. Maxey, Inter- and intragranular stresses in cyclically deformed 316 stainless steel, Mater. Sci. Eng. A 399 (2005) 114-119.
- [41] T. Ungár, J. Gubicza, P. Hanák, I. Alexandrov, Densities and character of dislocations and size-distribution of subgrains in deformed metals by X-ray diffraction profile analysis, Mater. Sci. Eng. A 319-321 (2001) 274-278.
- [42] T. Ungar, A. Borbely, The effect of dislocation contrast on X-ray line broadening: A new approach to line profile analysis, Appl. Phys. Lett. 69 (1996) 3173.
- [43] Z.Y. Zhong, H.-G. Brokmeier, W.M. Gan, E. Maawad, B. Schwebke, N. Schell, Dislocation density evolution of AA 7020-T6 investigated by *in-situ* synchrotron diffraction under tensile load, Mater. Charact. 108 (2015) 124-131.
- [44] M. Wilkens, The determination of density and distribution of dislocations in deformed single crystals from broadened X-ray diffraction profiles, Phys. Stat. Sol. A 2 (1970) 359-370.
- [45] T. Ungár, I. Dragomir, Á. Révész, A. Borbély, The contrast factors of dislocations in cubic

- crystals: the dislocation model of strain anisotropy in practice, J. Appl. Cryst. 32 (1999) 992–1002.
- [46] A.J. Zaddach, C. Niu, C.C. Koch, D.L. Irving, Mechanical properties and stacking fault energies of NiFeCrCoMn high-entropy alloy, JOM 65 (2013) 1780-1789.
- [47] J. Moon, S.I. Hong, J.W. Bae, M.J. Jang, D. Yim, H.S. Kim, On the strain rate-dependent deformation mechanism of CoCrFeMnNi high-entropy alloy at liquid nitrogen temperature, Mater. Res. Lett.5 (2017) 472-477.
- [48] G. Laplanche, A. Kostka, O.M. Horst, G. Eggeler, E.P. George, Microstructure evolution and critical stress for twinning in the CrMnFeCoNi high-entropy alloy, Acta Mater. 118 (2016) 152-163.
- [49] M.R. Daymond, M.A.M. Bourke, R.B. Von Dreele, B. Clausen, T. Lorentzen, Use of Rietveld refinement for elastic macrostrain determination and for evaluation of plastic strain history from diffraction spectra, J. Appl. Phys. 82 (1997) 1554-1562.
- [50] C. Sun, D.W. Brown, B. Clausen, D.C. Foley, K.Y. Yu, Y. Chen, S.A. Maloy, K.T. Hartwig, H. Wang, X. Zhang, *In-situ* neutron diffraction study on temperature dependent deformation mechanisms of ultrafine grained austenitic Fe-14Cr-16Ni alloy, Int. J. Plast. 53 (2014) 125-134.
- [51] D. Hull, D. J. Bacon, Introduction to Dislocations, 5th ed. Elsevier, 2011.
- [52] A.H. Cottrell, Dislocations and Plastic Flow in Crystals, Clarendon, 1954.
- [53] J. P. Hirth, J. Lothe, Theory of dislocations, 2nd ed. John Wiley & Sons, 1983.
- [54] J.S. Jeong, W. Woo, K.H. Oh, S.K. Kwon, Y.M. Koo, *In-situ* neutron diffraction study of the microstructure and tensile deformation behavior in Al-added high manganese austenitic steels,

Acta Mater. 60 (2012) 2290-2299.

- [55] T. Cai, Z.J. Zhang, P. Zhang, Competition between slip and twinning in face-centered cubic metals, *J. Appl. Phys.* 116 (2014) 163512.
- [56] B.E. Warren, Single and double deformation faults in face centered cubic crystals, *J. Appl. Phys.* 34 (1963) 1973-1975.
- [57] R.E. Smallman, K.H. Westmacott, Stacking faults in face-centered cubic metals and alloys, *Philos. Mag.* 2 (1957) 669-683.
- [58] R.P. Reed, R.E. Schramm, Relationship between stacking-fault energy and X-ray measurements of stacking-fault probability and micro-strain, *J. Appl. Phys.* 45 (1974) 4705-4711.
- [59] D. Balzar, H. Ledbetter, Voigt-function modeling in Fourier analysis of size- and strain-broadened X-ray diffraction peaks, *J. Appl. Cryst.* 26 (1993) 97-103.